

Monotonic instability and overstability in two-dimensional electrothermohydrodynamic flow

Yifei Guan¹,^{ORCID} Xuerao He,² Qi Wang,³ Zhiwei Song³,^{ORCID} Mengqi Zhang,² and Jian Wu^{3,*}

¹*Department of Mechanical Engineering, Rice University, Houston, Texas 77005, USA*

²*Department of Mechanical Engineering, National University of Singapore,
9 Engineering Drive 1, 117575 Singapore*

³*Key Laboratory of Aerospace Thermophysics, School of Energy Science and Engineering,
Harbin Institute of Technology, Harbin 150001, People's Republic of China*



(Received 15 August 2020; accepted 22 December 2020; published 26 January 2021)

Electrothermohydrodynamic convection driven by strong unipolar charge injection in the presence of a stabilizing inverse thermal gradient between two parallel electrodes is investigated by a linear stability analysis and a numerical simulation. The generalized Schur decomposition is used to solve for the eigenvalues of the linearized system revealing the critical parameters. The two relaxation time lattice Boltzmann method coupled to a fast Poisson solver is used to resolve the nonlinear system for the spatiotemporal distribution of flow field, electric field, charge density, and temperature. With strong charge injection and high electric Rayleigh number, the system exhibits electrothermoconvective vortices. The interactions between the stabilizing buoyancy force and the destabilizing electric force lead to overstability, where the flow constantly oscillates when instability evolves. A two-stage bifurcation is observed for overstability near the threshold Rayleigh number with a significant change in phase and amplitude. The effects of ion mobility and thermal diffusivity are characterized by the ratio of the counteracting forces.

DOI: [10.1103/PhysRevFluids.6.013702](https://doi.org/10.1103/PhysRevFluids.6.013702)

I. INTRODUCTION

Convection is ubiquitous in fluid systems. Various flow patterns have been observed as a result of body forces acting on the fluid, e.g., thermal convection [1–8], electroconvection [9–17], Marangoni effects [18–20], and magnetohydrodynamic (MHD) convection [21–24]. The experimental observation on the onset of thermal convection in fluids was first reported by Bénard in 1900 [1]. To explain the empirical observation, Rayleigh introduced a nondimensional parameter (referred to as the Rayleigh number), Ra , which determines the stability of a layer of fluid heated from below [2]. Ra can be viewed as the ratio of buoyancy and viscous forces multiplied by the ratio of momentum and thermal diffusivities [25]. Thermal convection in a horizontal plane layer of fluid heated from below is thus also referred to as Rayleigh–Bénard Convection (RBC). On the other hand, electroconvection (EC) phenomenon was first reported by Taylor in 1966, describing a cellular convection in the liquid droplet [26]. Since then, EC has been observed in a large number of systems where the interaction of electrostatic force with fluids is present. In nonequilibrium electrohydrodynamic (EHD) systems [10–13,26–37], a poorly conductive leaky dielectric fluid acquires unipolar charge injection at the surface interface in response to the electric field. Charge transport in the fluid can trigger instabilities leading to the development of EC vortices. EC can be characterized by a nondimension parameter, T , referred to as the Taylor number or electric Rayleigh number [11,14,36]. Similar to Ra , T can be viewed as the ratio of electric and viscous forces.

*Corresponding author: jian.wu@hit.edu.cn

Complex multiphysics interactions occur in a dielectric liquid containing space charge when a thermal gradient and an electric field are simultaneously applied [38–43]. The interactions among viscous force, buoyancy force, and electric force extend the applications of instability and associated bifurcation theories [38]. The study of electrothermohydrodynamics (ETHD) originates from the attempts to model in the laboratory the geoconvective motions of the earth mantle [38,44]. Recent studies focus on the augmentation of heat transfer achieved by extra convection induced by electric field [41–43]. Insights into the complex multiphysics interactions are essential for understanding the ETHD phenomena. These include (1) the temperature gradient from the difference between two constant temperature reservoirs; (2) the electric field from the potential difference between the anode and cathode and its modifications by the distribution of space charge; (3) the ions’ drift due to the electrical field; (4) the interaction between the motion of ions and the neutral molecules; and (5) the inertial and viscous forces in the complex flow. In addition, the nonlinearity induced by the varying physical properties dependent on the temperature and electric fields may affect the coupling and interactions. The ETHD convection was experimentally shown by Atten *et al.*, who observed that the Nusselt number (Nu), the ratio of convective and conductive heat transfer, depends on the applied electric field intensity [45]. Traoré *et al.* solved the coupled ETHD system, including the Navier-Stokes equations, the charge-density conservation, Poisson’s equation for electric potential, and the energy equation numerically, using a finite-volume method. They found that a subcritical bifurcation with varying Ra coexists with supercritical behavior with varying T , while the opposite is true for the corresponding pure problems [46]. Dantchi *et al.* simulated the ETHD in a 2D cavity and found that Nu can be independent of Ra for large T [47]. Wu and Traoré developed a total variation-diminishing (TVD) scheme to solve the convection-dominating charge-density equation and evaluated the heat transfer enhancement in a bounded cavity filled with silicone oil [35]. With the TVD scheme-based finite-volume solver, Wu *et al.* investigated the stability of the ETHD in a plane layer of dielectric liquid subjected to a destabilizing thermal gradient. The authors showed that the neutral stability curve is independent of the Prandtl number, Pr , and the nondimensional mobility number, M , while the linear bifurcation and the finite-amplitude stability criterion depends on Pr and M [48]. Additional to parallel plates, the ETHD phenomenon also exists in other geometries, such as the concentric or eccentric annuli [41,49]. More recently, Lu *et al.* investigated the ETHD within a square cavity and found that the enhancement of heat transfer by the electric field is more efficient for large Pr at small M and relatively small Ra [50]. Li *et al.* showed that the stably oscillating RBC at high Ra could be fully suppressed by EC driven by a strong electric field [42]. To investigate the effect of charge injection, Li *et al.* performed numerical analysis using a lattice Boltzmann model (LBM). The authors found that the charge injection affects the temperature and charge-density distribution, as well as the evolution of flow motion, especially for the case of larger T [51]. In a recent study, Li *et al.* identified three routes to the chaos of ETHD system in a square cavity [43].

The stability of convective flow systems is often analyzed with modal analysis, which assumes all dependent variables proportional to a factor $e^{\sigma t}$ after the initial perturbation is applied [11,52,53]. When σ is real, the critical point is taken at marginal stability $\sigma = 0$ corresponding to a neutral perturbation [52,53]. Most of the previous stability analyses of RBC, EC, and ETHD are focused on the conditions where σ is real. When σ is complex, however, the corresponding perturbation will become oscillatory. For $\text{Re}(\sigma) > 0$, the initial perturbation becomes an exponentially amplifying oscillation or for $\text{Re}(\sigma) = 0$ neutral oscillation, where $\text{Re}(\cdot)$ means the “real part of” [52–54]. This behavior is named “overstability” by Eddington [55]. In RBC, the possibility that σ may be complex was first noted by Rayleigh [2]. Chandrasekhar [56,57], Chandrasekhar and Elbert [58], and Veronis [59] have shown theoretically, and Fultz *et al.* [52,60] have shown by experiments that the overstable oscillating instability can be amplified in a layer of fluid uniformly heated from below and subject to Coriolis forces [61]. Overstability in more complicated RBC systems was found in MHD systems by Chandrasekhar [62,63] and Nakagawa [64,65], in viscoelastic fluid layers by Vest and Arpaci [66] and Khayat [67], and in nematic homeotropic films by Guyon *et al.* [68]. In other fluid-flow systems, Melcher and Schwarz Jr. showed that charge relaxation could produce overstability to the electromechanical polarization surface wave between insulating fluids

[69]. Jukes [70] and Moiseev and Sagdeev [71] have shown overstability in an inhomogeneous plasma, and Chen addressed that the overstability induces low-frequency oscillations and sets a limit to the confinement time of a plasma [72]. Overstability is also investigated in astrophysics, such as accretion disks [73] and sunspots [74,75].

In the ETHD flow, overstability is shown in systems with a destabilizing thermal gradient (heated from below) [76] or stabilizing thermal gradient (heated from above) [77]. For the latter, overstability can be predicted by the numerical models which consider the residual conductivity or the temperature-dependent physical properties. Pontiga *et al.* performed linear stability analysis and showed that the overstability in ETHD is caused by the restoring forces provided by a thermal gradient. The indirect coupling between the charge density and the thermal field through mobility and permittivity induces the oscillation [38]. The nonlinear analysis of ETHD stability was first performed using a reduced-order model analogous to the Lorenz system [78] by Il'in and Smorodin [79]. The authors found two classes of synchronous oscillatory modes in such systems. The authors later performed a direct numerical simulation using the finite-difference method and showed that with an increasing Ra , the critical T for oscillatory mode decreases while the one for the monotonic mode increases [80]. Taraut and Smorodin found that when the stabilizing thermal gradient is applied, the flow system evolves from the monotonic mode to the oscillatory mode via a transition in frequency [81]. Mordvinov and Smorodin showed that for relatively weak heating from above (low Ra), the initial perturbation either decays in an oscillatory manner (low T) or grows monotonically (large T). For a large Ra , however, an oscillatory growth of the initial perturbation occurs at large T [39]. Smorodin and Taraut showed that the ETHD system with stabilizing thermal gradient becomes chaotic for large T [40]. These studies with stabilizing thermal gradient mainly consider weak charge injection.

To gain insight into the complexity of the ETHD flow, the problem can be investigated using numerical simulations. The earlier direct numerical simulation of EHD flow is performed using a finite-difference method [80] and finite-volume methods [46]. Luo *et al.* showed that a single-relaxation time lattice Boltzmann model (SRT LBM) could predict the linear and finite-amplitude stability criteria of the subcritical bifurcation [41–43,51,82,83] for both 2D and 3D ETHD flow scenarios. This unified SRT LBM transforms the elliptic Poisson equation to a parabolic advection-diffusion equation and introduces tuning coefficients to control the evolution of the electric potential, requiring additional subiterations at each time step. Two-relaxation time (TRT) LBM has the advantages of being more accurate and stable over the SRT LBM [84–88]. A segregated solver was proposed that combines a TRT LBM modeling of the fluid and charge transport, and a fast Fourier transform (FFT) Poisson solver for the electrical field [14].

A systematic understanding of the multiphysics effects on the flow instabilities in the ETHD system subjected to strong charge injection and stabilizing thermal gradient paves the way to sophisticated applications of such flows in real-world scenarios, e.g., thermal-fluids system control. The linear and nonlinear numerical analysis and parametrization can be extended to alike convection systems driven by counteracting forces. In this paper, we parametrize the 2D ETHD stability of a dielectric fluid between two parallel electrodes in the presence of strong unipolar injection, an external electric field, and a stabilizing thermal gradient. We perform linear stability analysis to determine critical values and extend the segregated TRT LBM solver [14] by including the energy equation. The transition between subcritical bifurcation and supercritical bifurcation corresponds to the transition between monotonic instability and overstability, which can be characterized by the Rayleigh number Ra and electric Rayleigh number T . A two-stage bifurcation is observed for overstability close to the threshold values Ra_c and T_c , involving changes in amplitudes and phases. The effects of thermal conductivity and ion mobility on the flow can be characterized by a ratio R_F of flow-destabilizing electric force and flow-stabilizing buoyancy force.

II. PHYSICAL MODEL AND GOVERNING EQUATIONS

We consider a kind of ETHD convection in a layer of an incompressible Newtonian dielectric liquid between two parallel planar electrodes with distance H ; see Fig. 1. The liquid is assumed to

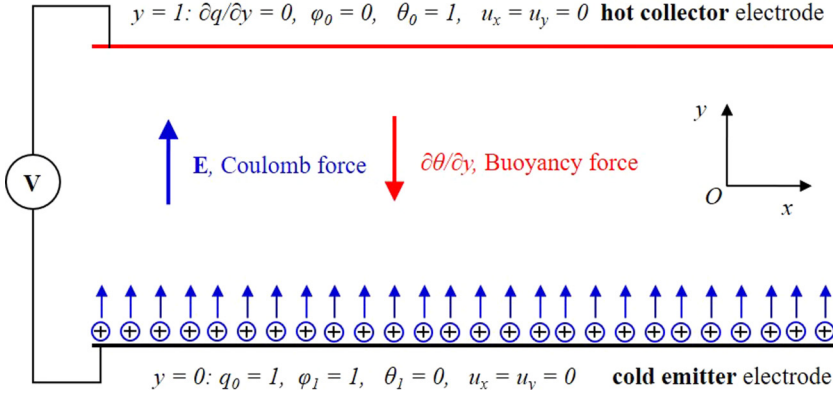


FIG. 1. Physical model and boundary conditions of ETHD convection in a layer of dielectric liquid. The external forces (Coulomb and buoyancy force) interact with viscous and inertial forces of the dielectric fluid, inducing convection after an initial perturbation.

be perfectly insulating, and it is affected by a direct-current electric field and a stabilizing thermal gradient simultaneously. The electric field and thermal gradient are modeled by constant voltages (φ) and temperatures (θ) at the upper (φ_0, θ_0) and lower electrodes (φ_1, θ_1). The lower electrode serves as the emitter electrode, and the upper one is a collector ($\varphi_1 > \varphi_0$). Positive ions are injected from the lower electrode ($q_0 = 1$) and collected by the upper electrode ($\partial q / \partial y = 0$). The unipolar injection is assumed to be homogeneous and autonomous, which means the injected charge density q is constant for the entire electrode and is not influenced by the local electric field and flow field [11,46]. Similarly, but opposite to the charge injection, the heat is introduced from the upper plate $\theta_0 > \theta_1$, establishing a stabilizing thermal gradient. Therefore, at the quiescent flow (hydrostatic) base state, the electric force (Coulomb force) and the buoyancy force are perpendicular to the electrodes, acting in the opposite direction. The two-dimensional flow field with aligned vortex pairs represents the rolling patterns in the three-dimensional counterpart. It can be obtained by perturbation with wave numbers in only one horizontal direction or by implementing a cross flow [16], given that cross flow does not interfere with the instabilities of the aligned vortices (in the same direction as the cross flow) [16]. The three-dimensional rolling pattern can be analyzed in a two-dimensional computational domain [12,42,89].

The governing equations for ETHD flow include the mass conservation equation, the Navier-Stokes equations with the electric and buoyancy forcing terms, the charge transport equation, the Poisson equation for electric potential, and the energy conservation equation. The viscous dissipation and Joule heating are neglected for simplicity [34,46]. Following the Boussinesq approximation [90], the governing equations can be written as [46,48]

$$\nabla \cdot \mathbf{u} = 0, \quad (1)$$

$$\rho_0 \left(\frac{\partial \mathbf{u}}{\partial t} + (\mathbf{u} \cdot \nabla) \mathbf{u} \right) = -\nabla p + \mu \nabla^2 \mathbf{u} + q \mathbf{E} - \rho_0 [\alpha_V (\theta - \theta_r)] \mathbf{g}, \quad (2)$$

$$\frac{\partial q}{\partial t} + \nabla \cdot [(\mathbf{u} + K \mathbf{E}) q - D \nabla q] = 0, \quad (3)$$

$$\nabla^2 \varphi = -\frac{q}{\varepsilon}, \quad (4)$$

$$\mathbf{E} = -\nabla \varphi, \quad (5)$$

$$\frac{\partial \theta}{\partial t} + \nabla \cdot (\mathbf{u} \theta) = k \nabla^2 \theta, \quad (6)$$

where $\mathbf{u} = (u_x, u_y)$, $\mathbf{E} = (E_x, E_y)$, and $\mathbf{g} = (0, -g)$, $g > 0$ denote fluid velocity, electric field, and the gravitational acceleration. The scalar variables p , q , φ , and θ stand for pressure, charge density, electric potential, and temperature. θ_r means the reference temperature, and it equals θ_1 in this study. The scalars ρ , μ , α_V , and k are the density, dynamic viscosity, coefficient of volumetric expansion, and thermal conductivity of the liquid. The scalars K , D and ε are the ionic mobility, charge diffusion coefficient, and the electrical permittivity of liquid. The ionic mobility K and electrical permittivity ε are assumed to be constant, independent of temperature and electric field. The dependence of fluid density, permittivity, and ionic mobility on temperature can be approximated by linear functions [35,80,91,92]. In this work, we assume these properties to be invariant, given the range of Ra as used in recent studies [39,43,93]. Therefore, the system is governed by the interaction between the Coulomb force, buoyancy force, and the viscous force of the fluids.

The system can be nondimensionalized with the electric field and thermal properties. The following transformation scales are considered: the length x and y are nondimensionalized by H , velocity \mathbf{u} by the drift velocity $u_{\text{drift}} = K(\varphi_1 - \varphi_0)/H$, $\nu = \mu/\rho_0$ being the kinetic viscosity, time t by $H^2/K(\varphi_1 - \varphi_0)$, charge density q by q_0 , electric potential φ by $(\varphi_1 - \varphi_0)$, temperature θ by $(\theta_0 - \theta_1)$, and pressure p by $\rho_0(\nu/H^2)$. The resulting nondimensional form of the governing equations [Eqs. (1)–(4)] is (for simplicity, we use the same form of symbols as only the nondimensional variables are considered in the later sections)

$$\nabla \cdot \mathbf{u} = 0, \quad (7)$$

$$\frac{\partial \mathbf{u}}{\partial t} + (\mathbf{u} \cdot \nabla) \mathbf{u} = -\nabla p + \frac{M^2}{T} \nabla^2 \mathbf{u} + CM^2 q \mathbf{E} + \frac{M^4 Ra}{T^2 Pr} \theta \mathbf{e}_z, \quad (8)$$

$$\frac{\partial q}{\partial t} + \nabla \cdot \left[(\mathbf{u} + \mathbf{E}) q - \frac{1}{Fe} \nabla q \right] = 0, \quad (9)$$

$$\nabla^2 \varphi = -Cq, \quad (10)$$

$$\mathbf{E} = -\nabla \varphi, \quad (11)$$

$$\frac{\partial \theta}{\partial t} + \nabla \cdot (\mathbf{u} \theta) = \frac{M^2}{T Pr} \nabla^2 \theta. \quad (12)$$

These nondimensional governing equations yield six nondimensional parameters describing the system's state [46,48]:

$$T = \frac{\varepsilon(\varphi_1 - \varphi_0)}{\mu K}, \quad C = \frac{q_0 H^2}{\varepsilon(\varphi_1 - \varphi_0)}, \quad M = \frac{(\varepsilon/\rho_0)^{1/2}}{K},$$

$$Fe = \frac{K(\varphi_1 - \varphi_0)}{D}, \quad Ra = \frac{g \alpha_V (\theta_0 - \theta_1) H^3}{k \nu}, \quad Pr = \frac{\nu}{k}.$$

The first four parameters are concerned with the electrical aspect of the problem. The electric Rayleigh number T is defined as the ratio between the Coulomb force and the viscous force. The injection strength parameter C measures the amount of injected charges. A strong charge injection ($C \approx 10$), as compared to the weak charge injection ($C \approx 0.1$), can distort the applied electric field by the space-charge effect, leading to a strong convection flow and high nonlinearity of the system. The mobility parameter M is the ratio between the hydrodynamic mobility $(\varepsilon/\rho_0)^{1/2}$ and ionic mobility. Fe is the dimensionless charge-diffusion parameter, and its typical value ranges between 10^3 and 10^4 [11,46]. The last two parameters are the Rayleigh number Ra and Prandtl number Pr , which are concerned with the thermal aspect of the problem. The values of Pr and M depend only on the fluid. For dielectric liquids, $Pr \geq 1$ and $M \geq 3$ [43,46,51].

The dimensionless boundary conditions are depicted in Fig. 1. The system is considered to be infinite in the horizontal direction (x direction), and therefore the periodic boundary condition for all

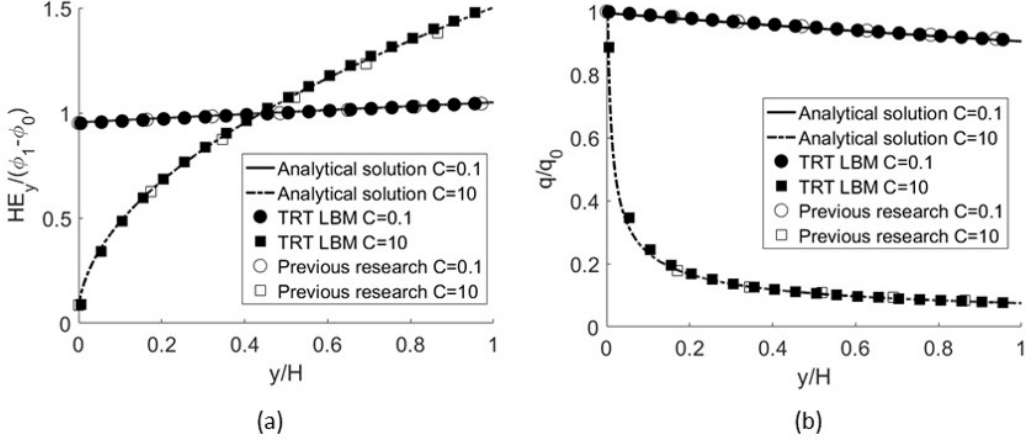


FIG. 2. Hydrostatic base state of the TRT LBM and Fast Poisson solver, unified SRT LBM [12], and the analytical solution [94,95] for $C = 0.1$ and $C = 10$, $Fe = 4000$. (a) Electric field and (b) charge density.

variables is applied. The two electrodes are assumed to be impermeable, electrically and thermally perfectly conducting, so the no-slip condition for velocity is applied. The Neumann boundary condition for charge density on the collection electrode means that the ions instantaneously discharge once they reach the electrode [11,46,48].

Figure 2 compares the one-dimensional hydrostatic base-state solutions for electric field and charge density among the analytical solution [94,95], the unified model of Luo *et al.* [12,13], and the TRT LBM [14]. The analytical solution is derived from a reduced set of equations for the electric field in one-dimensional coordinates.

$$q = \rho_a(y + y_a)^{-1/2}, \quad (13)$$

$$E_y = \frac{2\rho_a}{\varepsilon}(y + y_a)^{1/2}, \quad (14)$$

where ρ_a and y_a depend on the geometry configuration and boundary conditions. The injection parameter C determines the hydrostatic base state [11,36]. The temperature base state (not shown) is a linear profile due to the pure thermal diffusion.

III. LINEAR STABILITY ANALYSIS

To perform the linear stability analysis of the dimensionless fluid system [Eqs. (7)–(12)], we extend our previous method for the electroconvection [11] to electrothermohydrodynamic convection. All the state variables are decomposed into the base state and perturbation, i.e., $\mathbf{u} = \bar{\mathbf{u}} + \mathbf{u}'$, $p = \bar{p} + p'$, $\mathbf{E} = \bar{\mathbf{E}} + \mathbf{E}'$, $q = \bar{q} + q'$, $\phi = \bar{\phi} + \phi'$, and $\theta = \bar{\theta} + \theta'$. For two-dimensional space coordinates of the vector field, $\mathbf{u} = (u_x, u_y)$ and $\mathbf{E} = (E_x, E_y)$. Without a cross flow, the base state is hydrostatic and therefore $\bar{\mathbf{u}} = 0$. The base state of the thermal field is a linear function in y , i.e., $\bar{\theta} = y/H$. The base state of the electric field can be obtained by solving the 1D electrical conduction problem [Eqs. (9)–(11)] with $\mathbf{u} = 0$ [11,16] (see Fig. 2). For a modal analysis, the perturbation state variables can be further decomposed into waveform modes:

$$[\mathbf{u}', p', \mathbf{E}', \phi', \theta'] = [\tilde{\mathbf{u}}, \tilde{p}, \tilde{\mathbf{E}}, \tilde{\phi}, \tilde{\theta}] \exp(-i\omega t + i\alpha x), \quad (15)$$

where variables with tildes denote the shape function, which is a function of y , and α is the wave number in the x direction. $\omega = \omega_r + i\omega_i$ is the frequency of the perturbation. The real part ω_r represents the phase velocity, and the imaginary part ω_i represents the growth rate of the linear

perturbation. For the linearized system of ETHD, where the base state is hydrostatic, the eigenvalues of the oscillatory modes are in complex-conjugate pairs, which can be interpreted by the symmetry of the system (see Supplemental Material [96]). Additionally, if $\omega_r > 0$, the perturbation propagates towards the x direction. Otherwise, if $\omega_r < 0$, the propagation direction is reversed. Moreover, the traveling speed can be calculated as $u_p = \omega_r/\alpha$. If $\omega_r = 0$, the phase speed equals zero and the perturbation will decay or increase monotonically; otherwise, it will behave in an oscillatory manner. If $\omega_i > 0$, the perturbation will grow exponentially inducing convective flow patterns; otherwise, the perturbation will decay, and the flow will return to the base state. When $\omega_i = 0$, the system is in a neutral stability state and the corresponding dimensionless variables describing this state are the critical values.

The linearized governing equation can be derived by substituting the decomposed variables back to the dimensionless system [Eqs. (7)–(12)], subtracting the base-state equations, and truncating the higher-order terms:

$$\nabla \cdot \mathbf{u}' = 0, \quad (16)$$

$$\frac{\partial \mathbf{u}'}{\partial t} + \bar{\mathbf{u}} \nabla \mathbf{u}' + \mathbf{u}' \nabla \bar{\mathbf{u}} = -\nabla p' + \frac{M^2}{T} \nabla^2 \mathbf{u}' + CM^2(q' \bar{\mathbf{E}} + \bar{q} \mathbf{E}') + \frac{M^4 Ra}{T^2 Pr} \theta' \mathbf{e}_z, \quad (17)$$

$$\frac{\partial q'}{\partial t} + \nabla \cdot \left[(\mathbf{u}' + \mathbf{E}') \bar{q} + (\bar{\mathbf{E}}) q' - \frac{1}{Fe} \nabla q' \right] = 0, \quad (18)$$

$$\nabla^2 \varphi' = -Cq', \quad (19)$$

$$\mathbf{E}' = -\nabla \varphi', \quad (20)$$

$$\frac{\partial \theta'}{\partial t} + \nabla \cdot (\mathbf{u}' \bar{\theta}) = \frac{M^2}{T Pr} \nabla^2 \theta'. \quad (21)$$

The boundary conditions for the perturbation variables are

$$\bar{\mathbf{u}}(0, 1), \bar{\varphi}(0, 1), \bar{\theta}(0, 1), \bar{q}(0) = 0, \partial \bar{q} / \partial y(1) = 0. \quad (22)$$

The linearized dimensionless governing equations can be written symbolically as

$$\frac{d\gamma}{dt} = \mathbf{L}\gamma, \quad (23)$$

where γ is the vector of unknowns, and \mathbf{L} is the linear differential operator. For a wave-form γ [Eq. (15)], the linear system can be reformed as a generalized eigenvalue problem:

$$-i\omega\gamma = \mathbf{L}\gamma. \quad (24)$$

The eigenvalue problem [Eq. (24)] was discretized using the Chebyshev collocation method and solved using the MATLAB *eig* routine based on a QZ factorization [11], yielding the eigenvalues equal to $-i\omega$. The characteristics of ω unravel the linear stability properties of the original nonlinear ETHD flow system. From linear stability analysis, we obtain the critical values of Ra and T corresponding to critical wavelength $Lx = 2\pi/\alpha$. The critical wavelength is later used to determine the periodic computational domain.

For charge injected from the upper wall, the linearized governing equations [Eqs. (16)–(21)] remains the same as the charge injected from the lower wall used in this work (details in Supplemental Material [96]). Therefore, the stability threshold values are not affected by the charge injection direction, i.e., Ra_c and T_c remain the same whether charge is injected from the upper wall or the lower wall. In this paper, we focus on the charge injected from the lower wall.

To validate the results of linear stability analysis, we compare critical values of T at different Ra for the scenario where the ETHD system is heated from the lower electrodes, as shown in Table I.

TABLE I. Critical values of T (T_c) at different Ra for ETHD system heated from the lower wall at $C = M = 10$, $Fe = 10^6$ in the present study and $Fe = \infty$ (zero charge diffusion) in the paper by Rodriguez-Luis *et al.* [97].

Ra	T_c (Present study)	T_c [97]	Relative error
0	164.04	164.04	0
400	132.56	132.43	0.098%
800	95.10	95.23	0.14%

The previous study by Rodriguez-Luis *et al.* excluded the effect by the finite charge diffusivity [97]. For $Fe > 10^4$, this effect on the critical values can be negligible [11]. However, as $Fe = 1000$ is used for most of the results, we include the effects of charge diffusion in our study.

IV. NUMERICAL METHODS AND CONDITIONS

The TRT LBM approach is used to solve the transport equations for fluid flow, charge density, and temperature, coupled to a fast Poisson solver for electric potential [14,15]. The physical constants are determined by the nondimensional parameters, while the numerical code is in SI units. The numerical method is implemented in C++ using CUDA GPU (graphics processing units) computing. The number of threads in the x direction in each GPU block is equal to NX (number of grid points in x); the number of GPU blocks in the y direction is equal to NY (number of grid points in y). FFT and inverse fast Fourier transform (IFFT) operations are performed using the CUFFT library [98]. All variables are computed with double precision to reduce truncation errors. The numerical method was shown to be second-order accurate in space. To reduce computational cost while maintaining accuracy, the uniform grid of spacing $\Delta = 0.01$ is used throughout this work [14–16]. Table II specifies the macroscopic and mesoscopic boundary conditions. The no-slip boundary conditions are applied at both walls for fluid flow. A constant charge density at the anode (lower wall) represents a unipolar injection; a zero-diffusive flux condition $\partial q/\partial y = 0$ at the cathode (upper wall) represents an outflowing current. A constant electric potential is applied at the anode; the cathode is grounded ($\varphi = 0$). Constant temperatures are applied to upper and lower walls representing two thermal reservoirs. At mesoscale, the discrete distribution function of velocity $f_i(\mathbf{x}, t)$, charge density $g_i(\mathbf{x}, t)$, and temperature $h_i(\mathbf{x}, t)$ are used. The details on the transformations between macrovariables (\mathbf{u}, q, θ) and mesovariables (f_i, g_i, h_i) are presented in the Supplemental Material and can be found in recent publications [14,15,96]. The LBM full-way bounce-back (FBB) scheme is used for the Dirichlet (no-slip) boundary conditions for the fluid flow [12,13,99] and for charge density at the lower wall. The g_i Neumann boundary condition is set as a current outlet boundary condition for charge-density transport [12,13,100]. The grid convergence

TABLE II. Boundary conditions for the numerical simulations.

Boundary	Macrovariables conditions	Mesovariables conditions
x direction	Periodic	Periodic
Upper wall	$\mathbf{u} = 0, \varphi = 0, \partial q/\partial y = 0, \theta = \theta_0$	LBM FBB scheme for f_i [100–104] Neumann boundary condition $\partial g_i/\partial y = 0$ LBM FBB scheme for h_i [100–104]
Lower wall	$\mathbf{u} = 0, \varphi = \varphi_1, q = q_0, \theta = 0$	LBM FBB for f_i [100–104] LBM FBB for g_i [100–104] LBM FBB for h_i [100–104]

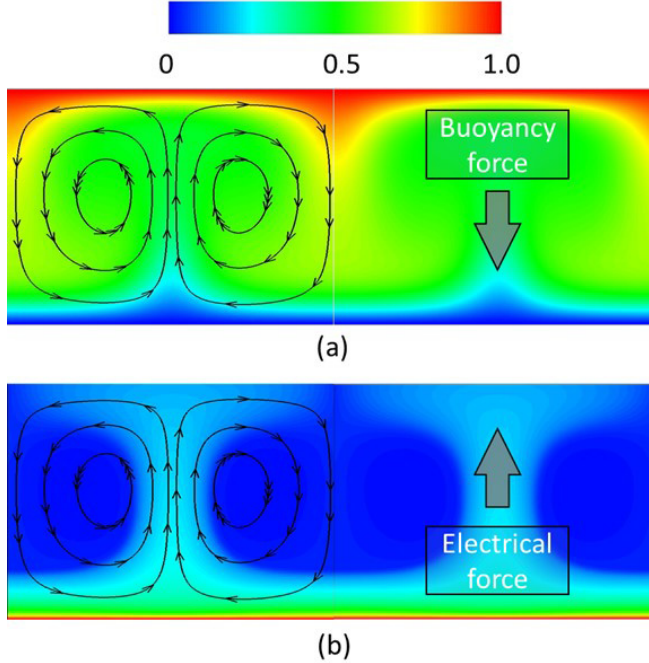


FIG. 3. Temperature (a) and charge-density (b) field of ETHD convection system heated from above. $C = M = Pr = 10$, $Ra = 977.6$, and $T = 230$ (monotonic mode). The computational domain is doubled periodically for visualization.

study provided in the Supplemental Material validates the second-order accuracy in both space and time [96].

To model EC vortices, the hydrostatic base state is perturbed using a small-amplitude waveform function that satisfies the boundary conditions and continuity equation:

$$\begin{aligned} u_x &= L_x \sin(2\pi y/L_y) \sin(2\pi x/L_x) \times \varepsilon \\ u_y &= L_y [\cos(2\pi y/L_y) - 1] \cos(2\pi x/L_x) \times \varepsilon. \end{aligned} \quad (25)$$

The physical domain size $L_y = 1$ and $L_x = 2\pi/\alpha$ is limited by the wave number α yielding the most unstable mode under various conditions. The perturbation amplitude, $\varepsilon = 10^{-3}$, is small enough to not affect the flow structures within the linear growth region [14,15]. The electric Nusselt number, $Ne = I/I_0$, serves as a flow stability and amplitude criterion, where I is the cathode current for a given solution and I_0 is the cathode current for the hydrostatic solution [13,34]; thus, if the EC vortices exist, $Ne > 1$. In the cases with strong ion injection, the ETHD convection stability largely depends on T and Ra ; in this analysis, furthermore, the effects of M and Pr are also investigated.

V. RESULTS AND DISCUSSION

ETHD convection occurs when the hydrostatic base state becomes an unstable equilibrium state with increasing T and Ra . Unlike the traditional Rayleigh-Bénard convection enhanced by electrical convection [43,51], where the most unstable mode is most likely monotonic, oscillatory modes (overstability) often exist when the system is heated from the upper wall (above). The monotonic mode is a characteristic of EC, while the oscillatory mode can be observed in thermal convection systems.

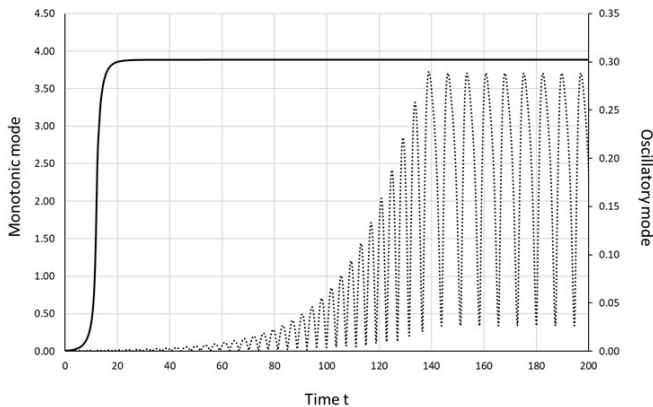


FIG. 4. Evolution of maximum u_y of monotonic (solid line) and oscillatory (dashed line) modes after initial perturbation at $C = Pr = M = 10$, $Fe = 2000$, $Ra = 977.6$, and $T = 225$.

Figure 3 shows the temperature and charge-density field of a representative ETHD system heated from above with a monotonic mode. One vortex pair exists in the computed period (half of the domain shown) driven by the electric force. In the classical EHD convection system, the charges drift from the anode (lower wall) to the cathode under the effect of the upward electric potential gradient. The up-drifting charges collide with the neutral molecules and transfer the electrical energy to kinetic energy. When the electric force is sufficiently large to overcome the viscous force ($T > T_c$), disturbance of the flow leads to a macroscale convective pattern. The convective patterns are composed of vortex pairs, which change the distribution of the charge-density field. The change in the charge-density field results in the change of the electric field due to the space-charge effect [Eq. (10)]. The three-way coupling can approach a static state under specified conditions. In addition to the three-way coupling, the ETHD system includes the effect of the buoyancy force resulting in a four-way coupling among the fluid flow, charge density, electric potential, and temperature. When the heat is applied to the cathode (upper wall), the temperature gradient is downward. Therefore, the downward buoyancy force counteracts with the upward electric force. The redistributed temperature field always acts in the opposite direction of the flow. In this case, the effect of the inverse thermal gradient can be regarded as a stabilizing temperature field.

Affected by the stabilizing thermal gradient, the ETHD system exhibits the feature of both monotonic instability and overstability (oscillatory mode). Figure 4 shows the time evolution of the maximum u_y after the initial perturbation is applied [Eq. (25)] for monotonic and oscillatory mode, at $C = Pr = M = 10$, $Fe = 2000$, $Ra = 977.6$, $T = 225$. The only difference is the wavelength used to perturb the flow, which are $Lx = 1.00$ and 1.40 for monotonic and oscillatory modes, respectively. The evolution of the monotonic mode starts with an exponential increase before the nonlinearities lead the flow to static equilibrium. The oscillatory mode, however, starts with an exponential increase with oscillation and ends up with a periodic oscillation. The initial evolution of both modes is consistent with the linear stability modal analysis. The maximum u_y of the monotonic mode is substantially larger than the oscillatory mode (note the different ranges of the velocity amplitude in the two vertical axes). The oscillating frequency of the overstability remains unchanged from the initial increase state to the equilibrium state.

A. Effects of Ra on the most unstable mode and bifurcation

To study the critical value T_c of the ETHD system, linear stability analysis is performed at $Pr = M = C = 10$ and $Fe = 2000$ for various Ra values. Figure 5 shows the T_c as a function of the perturbation wave number α . The neutral stability curves are obtained when $\text{Re}(-i\omega) = 0$. For

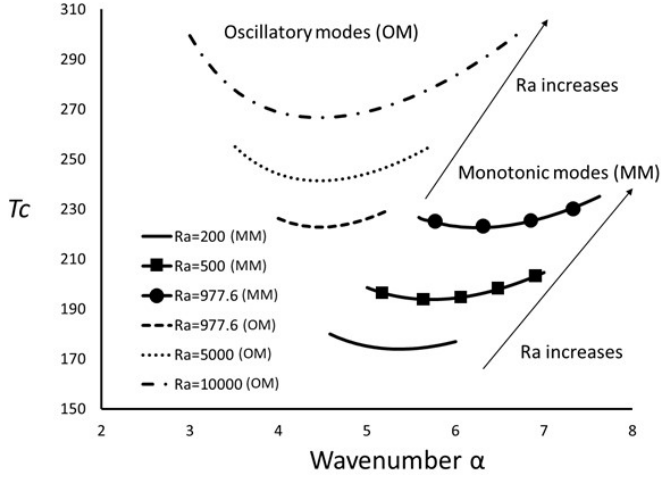


FIG. 5. Neutral stability curve (T_c vs wave number α) for monotonic modes (MM) and oscillatory modes (OM) at $Pr = M = C = 10$ and $Fe = 2000$.

$T > T_c$, the hydrostatic base state is unstable, and the initial perturbation with a wavelength equal to Lx grows exponentially, resulting in the ETHD convection flow patterns. Two scenarios are observed from linear stability analysis: monotonic mode (MM) at low Ra and oscillatory mode (OM) at high Ra . At low Ra , the flow system is characterized by the effect of EC, and the convective flow is mainly driven by the electric force. For an increasing Ra , the thermal forcing becomes significant, and therefore the threshold value of electric forcing (T_c) increases. At $Ra \approx 977.6$, OM occurs for low wave-number perturbation, and either OM or MM can exist. The resulting effect of either OM or MM depends on the smallest T_c at each curve. In particular, we found that $T_c = 222.7$ at $Ra = 977.6$ for both OM and MM. For further increasing values of Ra , the stabilizing thermal gradient exerts a strong forcing to the flow system, which becomes overstable. The change of wave number is accounted for in the numerical simulations by varying the domain length Lx .

Figure 5 shows either OM or MM can exist at $Ra = 977.6$ with the same T_c . In fact, at large Ra , OM and MM are both candidates of the ETHD instability of the corresponding wave numbers, as shown in Fig. 6. T_c grows linearly with respect to Ra with different ratios for OM and MM. Two curves cross at $Ra = 977.6$ where OM and MM have the same T_c . Although theoretically, either OM or MM can exist at large Ra , in reality the flow system is often perturbed by all wave numbers, and therefore, the mode with smaller T_c is the most unstable mode of the system. Since the most unstable mode changes from monotonic to oscillatory at $Ra = 977.6$, we denote this value as the critical Ra (Ra_c) of the ETHD system at $Pr = M = C = 10$ and $Fe = 2000$.

With the critical wavelength determined by the linear stability analysis, the critical value T_c can also be obtained from the numerical simulation. When T is slightly larger than T_c , the growth rate of any observables [$\text{Re}(-i\omega)$ in Eq. (24)] increases linearly with respect to T [13,34]. Therefore, the T_c can be approximated by the extrapolation of the $\text{Re}(-i\omega) \sim T$ curve. After the initial perturbation is applied, the maximum value u_y evolves exponentially with and without oscillation. The growth rate can be approximated by a linear fitting of the logarithm of the maximum u_y versus time. As shown in Fig. 7, the T_c from TRT LBM is extrapolated from three conditions for each case. The extrapolated values of T_c are close to the ones obtained from the linear stability analysis with a maximum relative error of 2.6%. T_c increases as Ra increases because, for a stabilizing thermal gradient, the buoyancy force counteracts the electric driving force.

In addition to the effects on the most unstable modes, the effect of Ra on the ETHD flow instability can also be investigated by the numerical simulation. Figure 8 shows bifurcation diagrams of the ETHD system, demonstrated by the electric Nusselt number Ne . When $T < T_c$,

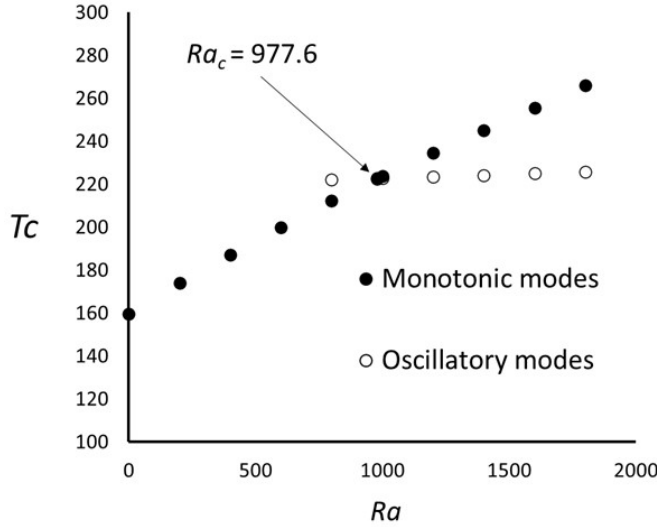


FIG. 6. Stability threshold T_c is proportional to Ra for ETHD system heat from above. The critical value of Ra (Ra_c) at $C = Pr = M = 10$ and $Fe = 2000$ marks the transition from monotonic instability to overstability.

the perturbation does not trigger the flow instability, and the perturbed flow evolves back to the hydrostatic base state ($Ne = 1$). If T decreases after the convection flow is established, the vortices are maintained until $T = T_f$ for monotonic modes. The difference between T_c and T_f forms a hysteresis loop, meaning that the bifurcation type is subcritical. For oscillatory mode, however, the convection flow can be maintained only if $T > T_c$ ($T_f = T_c$ for OM), meaning it is a supercritical bifurcation. The overstability of the ETHD exhibits two stages of bifurcation. When T is slightly higher than T_c , overstability occurs, and the oscillatory mode evolves at a constant frequency. When T is further increased, however, the second stage of bifurcation happens with a change of frequency and amplitude. The first stage of bifurcation corresponds to the linear bifurcation, where the linear

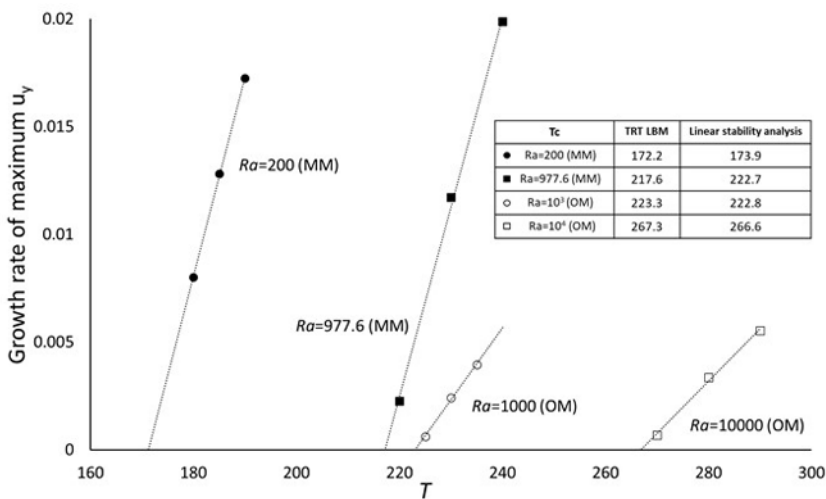


FIG. 7. Growth rate of the maximum u_y increases linearly with respect to T . T_c is approximated by linear extrapolation. $Pr = M = C = 10$ and $Fe = 2000$.

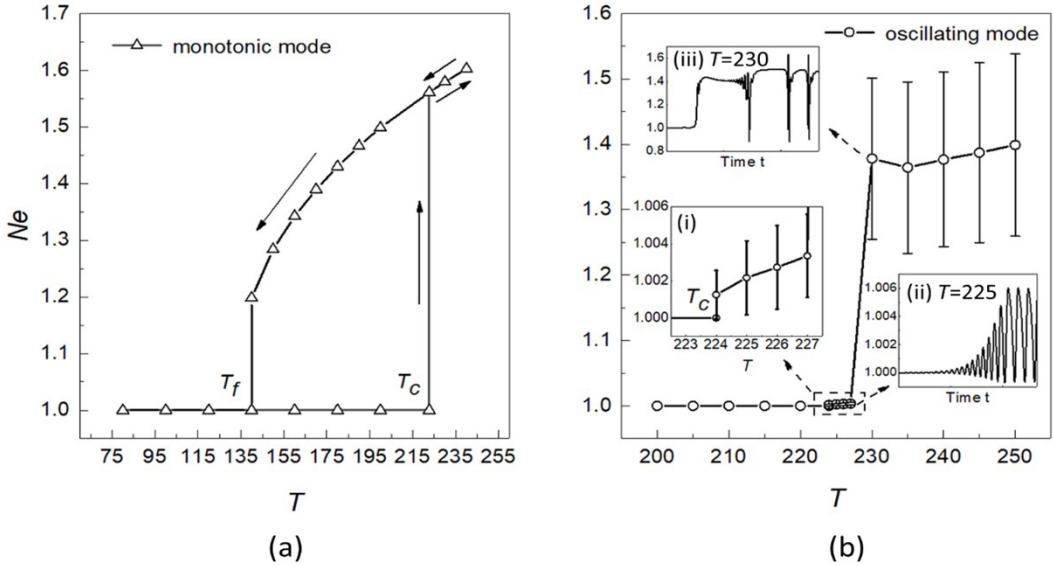


FIG. 8. Electric Nusselt number Ne vs T for $Ra = 977.6$, $Pr = M = C = 10$, and $Fe = 2000$ for (a) monotonic mode and (b) oscillatory mode. The bifurcation with respect to the monotonic mode is subcritical with a hysteresis loop, while the one for the oscillatory mode is supercritical. Overstability exhibits two stages of bifurcation. Panel (i) amplifies the first stage where the frequency remains unchanged. Panels (ii) and (iii) show the Ne evolution with time at the first and second stage, respectively. Linear stability analysis predicts the first stage of bifurcation. Error bars represent one standard deviation of the oscillation.

stability analysis predicted the threshold. The second stage can be attributed to the nonlinear effects of the ETHD flow system, which can also be observed by changing mobility and thermal diffusivity (see Figs. 13 and 14). The T_f of monotonic mode equals 140. From linear stability analysis shown in Fig. 6, $Ra = 977.6$ is the critical value Ra_c where the most unstable monotonic and oscillatory modes have the same T_c . Numerical analysis by TRT LBM shows that the Ra_c also determines the transition between subcritical (monotonic mode) and supercritical (oscillatory mode) bifurcations. Therefore, in the ETHD system heated from above, the monotonic mode emerges with a subcritical bifurcation ($Ra < Ra_c$), which is a feature of the classical EHD convection systems, and the oscillatory mode with supercritical bifurcation, which is a feature of the heat convection ($Ra > Ra_c$). The phenomenon can be interpreted by the magnitude of the buoyance force, i.e., the last term in Eq. (8). When Ra is large, the buoyancy force dominates, and the system exhibits behaviors commonly observed in thermal convection (supercritical bifurcation). Otherwise, the system exhibits behaviors as the classical EHD convection (subcritical bifurcation with a hysteresis loop).

The oscillatory modes at the first and second stages of bifurcation are illustrated in Figs. 9 and 10, respectively. At the first stage, the flow field contains a single wavelength oscillating at a constant frequency. As shown in Fig. 9, the temperature and charge-density fields exhibit an oscillatory mode with a constant wavelength equal to the initial perturbation (Lx). One vortex pair exists in the flow field characterizing the convection. The vortex pair switches position as the flow oscillates. The flow field is different from the monotonic mode (see Fig. 3), where a distinct upward charge-density channel drives the convection.

Figure 10 shows the temperature, charge-density and vorticity-field snapshots at the second stage of bifurcation for oscillatory modes. In this scenario, the flow field is similar to the monotonic mode (see Fig. 3) characterized by the distinct upward charge-density channels (light blue region in charge-density field). However, the flow field here is oscillating, and the charge-density channels can

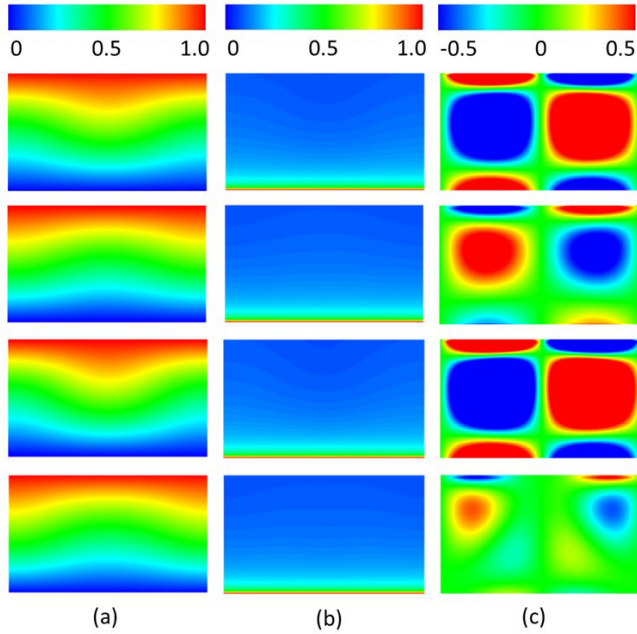


FIG. 9. Snapshots of (a) temperature, (b) charge density, and (c) vorticity field for $T = 225$, $Ra = 977.6$, $Pr = M = C = 10$, and $Fe = 2000$. The oscillatory mode is at the first stage of bifurcation, where the wavelength remains constant. (Full video is provided in the Supplemental Material. [96]).

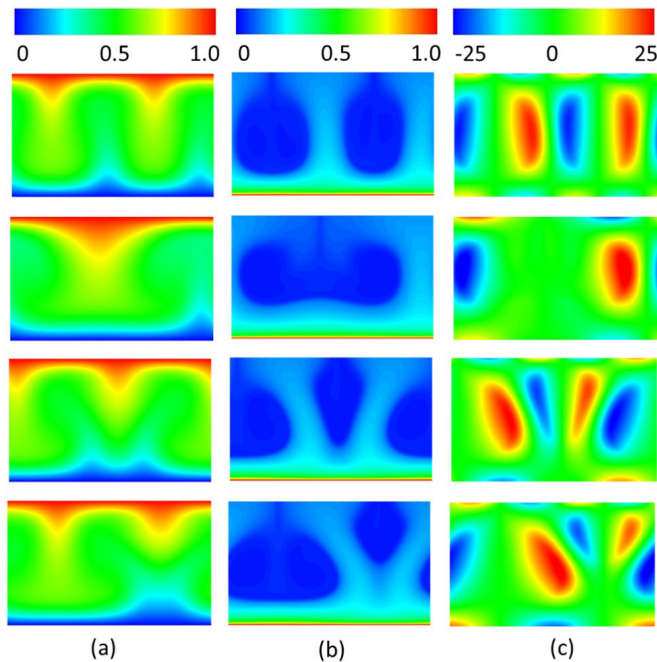


FIG. 10. Snapshots of (a) temperature, (b) charge density, and (c) vorticity field for $T = 245$, $Ra = 977.6$, $Pr = M = C = 10$, and $Fe = 2000$. The oscillatory mode is at the second stage of bifurcation, where multiple wavelengths coexist. (Full video is provided in the Supplemental Material. [96]).

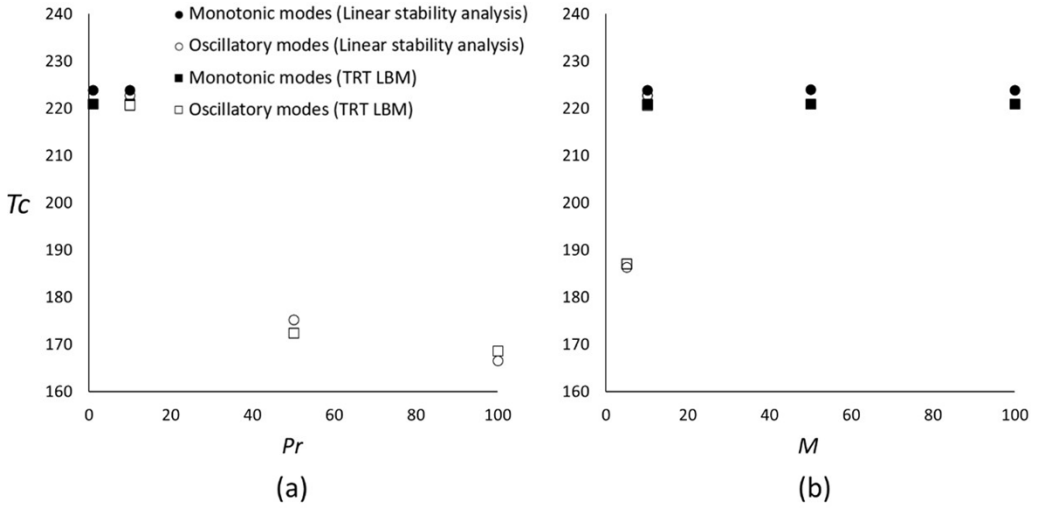


FIG. 11. Monotonic instability threshold T_c remains the same with varying Pr and M . Overstability threshold T_c decreases with increasing Pr or decreasing M .

merge and split into multiples. The flow field at the second stage is about two orders of magnitude larger than the one at the first stage, as indicated by the vorticity field. The irregular behaviors of the flow field lead to smaller wavelengths and higher frequencies. The animation files of Figs. 9 and 10 are available in the Supplemental Material [96].

In Sec. V A, we performed a linear stability analysis of the ETHD system and obtained the critical values T_c and the corresponding wave numbers. The wavelengths determined by the linear stability analysis are used in numerical simulations for flow stability analysis. For $C = Pr = M = 10$ and $Fe = 2000$, the critical value of $Ra_c = 977.6$ determines whether the most unstable mode of the system is monotonic or oscillatory (transition to overstability). Moreover, Ra_c indicates the transition between the subcritical and supercritical bifurcation of the ETHD system.

B. Effects of Pr and M on the flow stability

In addition to Ra , Pr and M can also affect the stability of the ETHD system. From the previous section, we found that the transition to overstability occurs at $Pr = M = 10$ and $Ra_c = 977.6$. In this section, we use $Ra = 1000$ and determine the effects of Pr and M on the critical value T_c . As shown in Fig. 11, the transition between monotonic and oscillatory most unstable mode occurs near $Pr = M = 10$. For a decreasing Pr or increasing M , the most unstable mode is monotonic. Contrarily, for an increasing Pr or decreasing M , the most unstable mode is oscillatory. T_c remains unchanged as Pr or M varies for monotonic modes. For oscillatory modes, however, T_c decreases as Pr increases or M decreases.

Figure 12 shows the effects of Pr and M on the monotonic modes of the ETHD system. Similar to the linear stability analysis shown in Fig. 11, T_c obtained from numerical simulation remains unchanged for different values of Pr and M . The critical value T_f corresponds to the finite-amplitude disturbance where the transition between a convective state to the hydrostatic base state occurs. The value of T_f is obtained from the numerical simulation where Ne decays to unity. The decreasing Pr and increasing M result in a larger T_f . The phenomenon can be explained by the dimensionless momentum equation, Eq. (8). The counteracting effect of electric and thermal forces

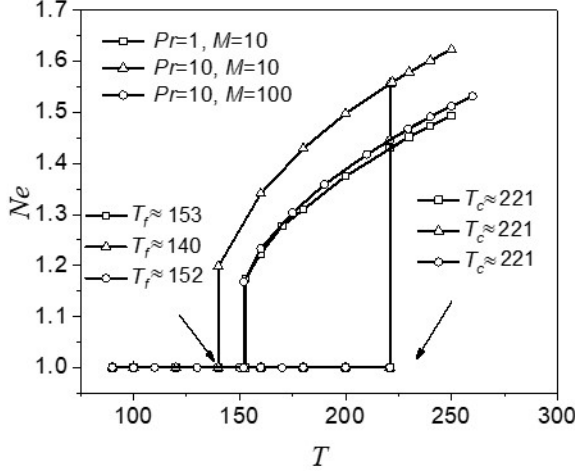


FIG. 12. Electric Nusselt number Ne vs T for monotonic modes at $Ra = 1000$, $C = 10$, and $Fe = 2000$. T_f increases for a decreasing Pr and an increasing M .

can be represented by the ratio of two forces:

$$\frac{|\mathbf{F}_{\text{electric}}|}{|\mathbf{F}_{\text{thermal}}|} = \frac{|CM^2q\mathbf{E}|}{\left|\frac{M^4Ra}{T^2Pr}\theta\mathbf{e}_z\right|} = \frac{CT^2Pr}{M^2Ra} \frac{|q\mathbf{E}|}{|\theta\mathbf{e}_z|}. \quad (26)$$

Since $|q\mathbf{E}|/|\theta\mathbf{e}_z| \sim O(1)$ for the dimensionless system, the forcing effect of the ETHD system mainly depends on the parameter

$$R_F = \frac{CT^2Pr}{M^2Ra} = \frac{q_0(V_1 - V_0)/H}{\rho_0 g \alpha_V (\theta_0 - \theta_1)}, \quad (27)$$

which can be interpreted as the ratio of the electric force to the thermal force. This parameter can be applied to ETHD system heated from above, where the electric force and the thermal force act in the opposite direction. A decreasing Pr or an increasing M leads to a decreasing R_F . Since the electric forcing drives the EC system, the thresholds increase as R_F decreases. Therefore, R_F can be used for the analysis of T_f of both OM ($T_f = T_c$ as in Fig. 11) and MM (Fig. 12). However, to predict T_c for MM and the transition between OM and MM, the full system should be considered in either linear stability analyses or numerical simulations.

Figure 13 shows the effect of M on the established oscillatory modes. The flow was disturbed at $Pr = M = 10$ with the critical wavelength and developed into an oscillating equilibrium. The parameter M was then reduced to $M = 8$ while other parameters and the domain size remained the same. The ETHD system evolved into a different equilibrium with a higher magnitude of velocity and a high frequency of oscillation. When M was further reduced after the different oscillating equilibrium was established, the system went through a nonlinear transition and eventually developed into a monotonic mode. The maximum u_y increases as M decreases because of an increasing R_F and therefore an increasing driving force. The phenomenon observed here is different from the analysis of T_c (Fig. 11), where large M tends to result in monotonic modes. This can be attributed to the different wavelengths used to constrain the ETHD system and the nonlinear effects after the convection flow patterns are established. Further decreasing M down to unity does not trigger overstability after monotonic mode is established.

Figure 14 shows the effects of Pr on the oscillatory mode. After the initial development of the flow field (same as in Fig. 13), the increasing value of Pr results in a different oscillation. The change of Pr from 10 to 12 excites various modes of the ETHD system, resulting in the multiple

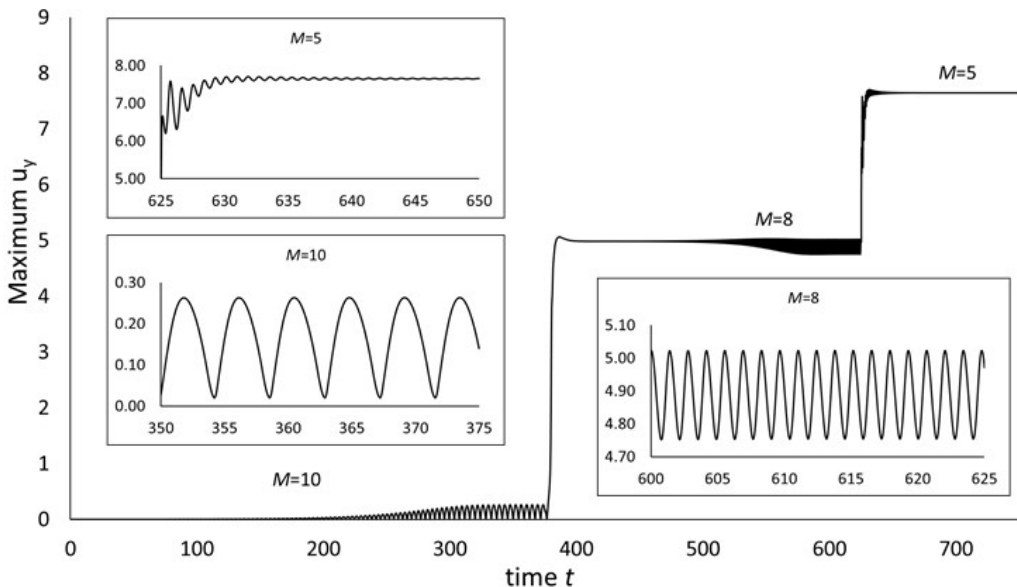


FIG. 13. Time evolution of maximum wall normal velocity u_y for varying M at $Ra = 1000$, $Pr = C = 10$, and $Fe = 2000$. The value is normalized by the u_{drift} at $M = 10$ for consistency. The embedded panels show the temporal structures of maximum u_y for each M .

frequencies oscillation. Further increasing Pr from 12 to 15, however, does not change the flow pattern distinctly. Although the time series of maximum u_y indicates a broadband spectrum when Pr is large, periodic pattern can be observed and the flow remains laminar. Further increasing Pr up to 100 does not change the oscillation pattern substantially.

In Sec. V B, we investigated the effects of M and Pr on the monotonic instability and overstability of the ETHD system. For monotonic modes, T_c does not depend on Pr or M . T_f increases as M increases, or Pr decreases, as R_F decreases. For oscillatory modes, $T_c = T_f$ decreases as M decreases or Pr increases, as R_F increases. After the oscillatory modes are established, decreasing M leads to a monotonic mode, and increasing Pr results in oscillation with multiple phases.

VI. CONCLUSION

The 2D numerical study extends the EC stability analysis to ETHD flow between two infinitely long parallel electrodes with unipolar charge injection and inverse thermal gradient. The system can exhibit either monotonic instability or overstability (oscillatory instability). Linear stability modal analysis predicts the threshold parameters for both monotonic and oscillatory instabilities. The numerical approach utilizes the TRT LBM to solve the flow, charge, and energy transportation and a fast Poisson solver to solve for the electric field. For a strong charge injection, the electric force destabilizes the no-flow base state and drives the convection. The inverse thermal gradient is implemented in the opposite direction of the flow and acts as a stabilizing force. When the thermal stabilizing effect is weak, the ETHD flow system exhibits monotonic instability similar to classical EC. When the Rayleigh number is larger than the critical value ($Ra > Ra_c$), however, the ETHD flow system exhibits overstability. The bifurcation changes from subcritical to supercritical when overstability occurs.

The effects of ion mobility and thermal conductivity on the ETHD flow are investigated in terms of dimensionless parameters M and Pr . For monotonic instability, the linear threshold T_c is independent of M and Pr . T_f increases as M increases or Pr decreases as the ratio of electric

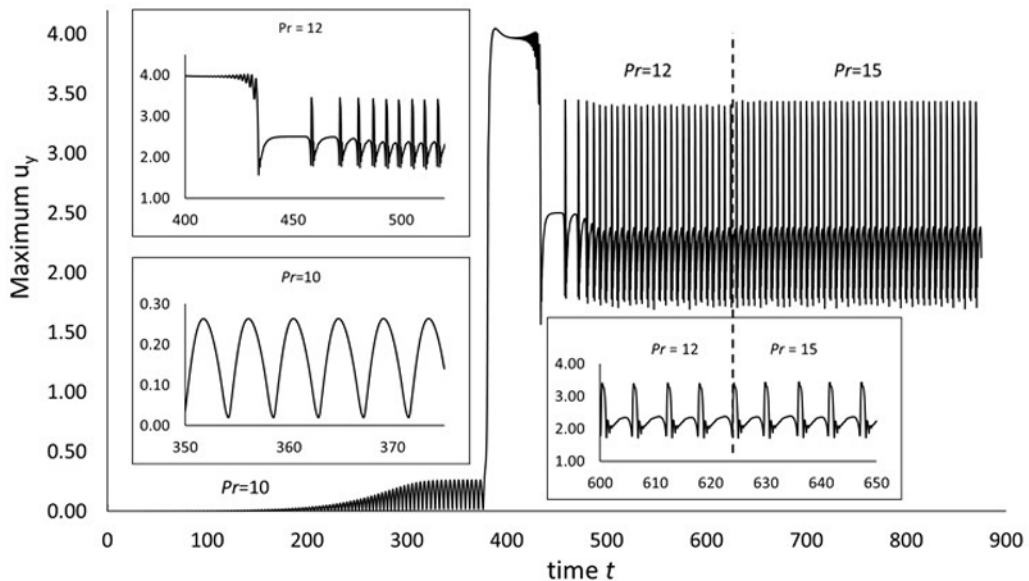


FIG. 14. Time evolution of maximum wall normal velocity u_y for varying Pr at $Ra = 1000$, $M = C = 10$, and $Fe = 2000$. The value is normalized by the u_{drift} at $Pr = 10$ for consistency. The embedded panels show the temporal structures of maximum u_y for each Pr .

to buoyancy force R_F decreases. For overstability, however, the linear threshold decreases as M decreases or Pr increases. Furthermore, a decreasing M leads to a change of phase of the oscillatory instability and eventually to a stable equilibrium (monotonic mode). An increasing Pr leads to a second bifurcation similar to the effect of an increasing T on the oscillatory instability near the threshold value T_c , where the ETHD flow exhibits multiple phases.

The linear and nonlinear numerical analyses shed light on the multiphysics of convection flow systems subjected to counteracting forces, which can be observed in atmospheric convection, solar magnetoconvection, and mantle convection. The analysis of the ETHD system can be applied to heat transfer and flow stability control in boiling, melting, and condensation. Future work can be focused on the route from overstability to chaos of ETHD system with a stabilizing thermal gradient. Generalization of the proposed methods and analysis to three-dimensional convective patterns, e.g., square patterns, hexagon patterns as in Ref. [16], is an ongoing research topic.

ACKNOWLEDGMENTS

J.W. appreciates the support from the National Natural Science Foundation of China (Grant No. 11802079) and the CAST-BISEE innovation fund (Grant No. 2019-012). M.Z. appreciates the Start-up Grant from the Ministry of Education, Singapore (MOE WBS No. R-265-000-619-133).

-
- [1] H. Bénard, Les tourbillons cellulaires dans une nappe liquide, *Rev. Gen. Sci. Pure Appl.* **11**, 10 (1900).
 - [2] L. Rayleigh, Convection currents in a horizontal layer of fluid, when the higher temperature is on the under side, *Philos. Mag.* **32**, 529 (1916).
 - [3] H. Jeffreys, The stability of a layer of fluid heated below, *Philos. Mag.* **2**, 833 (1926).
 - [4] A. P.-R. Southwell, On maintained convection in a fluid heated from below, *Proc. R. Soc. A* **176**, 32 (1940).

- [5] P. Bergé and M. Dubois, Rayleigh-Bénard convection, *Contemp. Phys.* **25**, 535 (1984).
- [6] E. L. Koschmieder, *Bénard Cells and Taylor Vortices* (Cambridge University Press, Cambridge, 1993).
- [7] P. G. Drazin and W. H. Reid, *Hydrodynamic Stability* (Cambridge University Press, Cambridge, 2004).
- [8] S. Chandrasekhar, *Hydrodynamic and Hydromagnetic Stability* (Courier Corporation, North Chelmsford, Massachusetts, USA, 2013).
- [9] P. Traoré and J. Wu, On the limitation of imposed velocity field strategy for Coulomb-driven electroconvection flow simulations, *J. Fluid Mech.* **727**, R3 (2013).
- [10] A. Pérez, P. Vázquez, J. Wu, and P. Traoré, Electrohydrodynamic linear stability analysis of dielectric liquids subjected to unipolar injection in a rectangular enclosure with rigid sidewalls, *J. Fluid Mech.* **758**, 586 (2014).
- [11] M. Zhang, F. Martinelli, J. Wu, P. J. Schmid, and M. Quadrio, Modal and non-modal stability analysis of electrohydrodynamic flow with and without cross-flow, *J. Fluid Mech.* **770**, 319 (2015).
- [12] K. Luo, J. Wu, H.-L. Yi, and H.-P. Tan, Lattice Boltzmann model for Coulomb-driven flows in dielectric liquids, *Phys. Rev. E* **93**, 023309 (2016).
- [13] K. Luo, J. Wu, H.-L. Yi, and H.-P. Tan, Three-dimensional finite amplitude electroconvection in dielectric liquids, *Phys. Fluids* **30**, 023602 (2018).
- [14] Y. Guan and I. Novosselov, Two relaxation time lattice Boltzmann method coupled to Fast Fourier Transform Poisson Solver: Application to electroconvective flow, *J. Comput. Phys.* **397**, 108830 (2019).
- [15] Y. Guan and I. Novosselov, Numerical analysis of electroconvection in cross-flow with unipolar charge injection, *Phys. Rev. Fluids* **4**, 103701 (2019).
- [16] Y. Guan, J. Riley, and I. Novosselov, Three-dimensional electroconvective vortices in cross flow, *Phys. Rev. E* **101**, 033103 (2020).
- [17] J. Huang, R. D. Selvakumar, Y. Guan, H. Li, P. Traoré, and J. Wu, Numerical investigation of injection-induced electro-convection in a dielectric liquid between two eccentric cylinders, *Int. J. Heat Fluid Flow* **83**, 108594 (2020).
- [18] C. Marangoni, *Sull'espansione delle gocce d'un liquido galleggianti sulla superficie di altro liquido* (Fratelli Fusi, Italy, 1865).
- [19] J. W. Gibbs, *On the Equilibrium of Heterogeneous Substances* (1879).
- [20] M. G. Velarde and R. K. Zeytounian, *Interfacial Phenomena and the Marangoni Effect* (Springer, Vienna, 2002).
- [21] N. Riley, Magnetohydrodynamic free convection, *J. Fluid Mech.* **18**, 577 (1964).
- [22] K. Pradhan and A. Guha, CFD solutions for magnetohydrodynamic natural convection over horizontal and vertical surfaces, *J. Mol. Liq.* **236**, 465 (2017).
- [23] M. Sheikholeslami and S. Shehzad, Magnetohydrodynamic nanofluid convection in a porous enclosure considering heat flux boundary condition, *Int. J. Heat Mass Transfer* **106**, 1261 (2017).
- [24] B. Shankar and I. Shivakumara, Magnetohydrodynamic stability of pressure-driven flow in an anisotropic porous channel: Accurate solution, *Appl. Math. Comput.* **321**, 752 (2018).
- [25] Y. Cengel, *Heat and Mass Transfer: Fundamentals and Applications* (McGraw-Hill Higher Education, New York, 2014).
- [26] G. I. Taylor, Studies in electrohydrodynamics. I. The circulation produced in a drop by an electric field, *Proc. R. Soc. London, Ser. A* **291**, 159 (1966).
- [27] D. C. Jolly and J. R. Melcher, Electroconvective instability in a fluid layer, *Proc. R. Soc. London, Ser. A* **314**, 269 (1970).
- [28] B. Malraison and P. Atten, Chaotic Behavior of Instability Due to Unipolar Ion Injection in a Dielectric Liquid, *Phys. Rev. Lett.* **49**, 723 (1982).
- [29] A. Castellanos and P. Atten, Numerical modeling of finite amplitude convection of liquids subjected to unipolar injection, *IEEE Trans. Ind. Appl.* **IA-23**, 825 (1987).
- [30] Z. A. Daya, V. B. Deyirmenjian, and S. W. Morris, Bifurcations in annular electroconvection with an imposed shear, *Phys. Rev. E* **64**, 036212 (2001).
- [31] K. Adamiak and P. Atten, Simulation of corona discharge in point-plane configuration, *J. Electrostat.* **61**, 85 (2004).

- [32] P. Tsai, Z. A. Daya, and S. W. Morris, Aspect-ratio Dependence of Charge Transport in Turbulent Electroconvection, *Phys. Rev. Lett.* **92**, 084503 (2004).
- [33] P. Tsai, Z. A. Daya, and S. W. Morris, Charge transport scaling in turbulent electroconvection, *Phys. Rev. E* **72**, 046311 (2005).
- [34] P. Traoré and A. Pérez, Two-dimensional numerical analysis of electroconvection in a dielectric liquid subjected to strong unipolar injection, *Phys. Fluids* **24**, 037102 (2012).
- [35] J. Wu and P. Traoré, A finite-volume method for electro-thermoconvective phenomena in a plane layer of dielectric liquid, *Numer. Heat Transfer, Part A* **68**, 471 (2015).
- [36] M. Zhang, Weakly nonlinear stability analysis of subcritical electrohydrodynamic flow subject to strong unipolar injection, *J. Fluid Mech.* **792**, 328 (2016).
- [37] K. Luo, J. Wu, H.-L. Yi, L.-H. Liu, and H.-P. Tan, Hexagonal convection patterns and their evolutionary scenarios in electroconvection induced by a strong unipolar injection, *Phys. Rev. Fluids* **3**, 053702 (2018).
- [38] F. Pontiga, A. Castellanos, and A. Richardson, The onset of overstable motions in a layer of dielectric liquid subjected to the simultaneous action of a weak unipolar injection of charge and a thermal gradient, *Q. J. Mech. Appl. Math.* **45**, 25 (1992).
- [39] A. Mordvinov and B. Smorodin, Electroconvection under injection from cathode and heating from above, *J. Exp. Theor. Phys.* **114**, 870 (2012).
- [40] B. Smorodin and A. Taraut, Dynamics of electroconvective wave flows in a modulated electric field, *J. Exp. Theor. Phys.* **118**, 158 (2014).
- [41] T.-F. Li, X.-R. He, K. Luo, and H.-L. Yi, Oscillatory flows of electro-thermo-convection in eccentric annulus, *Int. J. Heat Mass Transfer* **134**, 920 (2019).
- [42] T.-F. Li, K. Luo, and H.-L. Yi, Suppression of Rayleigh-Bénard secondary instability in dielectric fluids by unipolar charge injection, *Phys. Fluids* **31**, 064106 (2019).
- [43] T.-F. Li, Z.-G. Su, K. Luo, and H.-L. Yi, Transition to chaos in electro-thermo-convection of a dielectric liquid in a square cavity, *Phys. Fluids* **32**, 013106 (2020).
- [44] M. Gross and J. Porter, Electrically induced convection in dielectric liquids, *Nature (London)* **212**, 1343 (1966).
- [45] P. Atten, F. McCluskey, and A. Perez, Electroconvection and its effect on heat transfer, *IEEE Trans. Electr. Insul.* **23**, 659 (1988).
- [46] P. Traoré, A. Pérez, D. Koulova, and H. Romat, Numerical modelling of finite-amplitude electro-thermo-convection in a dielectric liquid layer subjected to both unipolar injection and temperature gradient, *J. Fluid Mech.* **658**, 279 (2010).
- [47] K. Dantchi, T. Philippe, R. Hubert, W. Jian, and L. Christophe, Numerical simulations of electro-thermo-convection and heat transfer in 2D cavity, *J. Electrostat.* **71**, 341 (2013).
- [48] J. Wu, P. Traoré, A. T. Pérez, and M. Zhang, Numerical analysis of the subcritical feature of electro-thermo-convection in a plane layer of dielectric liquid, *Phys. D* **311**, 45 (2015).
- [49] J. Wu, P. Traoré, M. Zhang, A. T. Pérez, and P. A. Vázquez, Charge injection enhanced natural convection heat transfer in horizontal concentric annuli filled with a dielectric liquid, *Int. J. Heat Mass Transfer* **92**, 139 (2016).
- [50] Z. Lu, G. Liu, and B. Wang, Flow structure and heat transfer of electro-thermo-convection in a dielectric liquid layer, *Phys. Fluids* **31**, 064103 (2019).
- [51] T.-F. Li, K. Luo, and H.-L. Yi, Effect of unipolar charge injection direction on the onset of Rayleigh-Bénard convection: A lattice Boltzmann study, *Int. Commun. Heat Mass Transfer* **112**, 104496 (2020).
- [52] D. Fultz, Y. Nakagawa, and P. Frenzen, An instance in thermal convection of Eddington's "Overstability", *Phys. Rev.* **94**, 1471 (1954).
- [53] P. J. Schmid, D. S. Henningson, and D. F. Jankowski, Stability and transition in shear flows. Applied mathematical sciences, Vol. 142, *Appl. Mech. Rev.* **55**, B57 (2002).
- [54] S. H. Strogatz, *Nonlinear Dynamics and Chaos with Student Solutions Manual: With Applications to Physics, Biology, Chemistry, and Engineering* (CRC Press, Boca Raton, 2018).
- [55] A. S. Eddington, The internal constitution of the stars, *Nature* **106**, 14 (1920).

- [56] S. Chandrasekhar, XLVI. On the inhibition of convection by a magnetic field, *London, Edinburgh Dublin Philos. Mag. J. Sci.* **43**, 501 (1952).
- [57] S. Chandrasekhar, The instability of a layer of fluid heated below and subject to Coriolis forces, *Proc. R. Soc. London, Ser. A* **217**, 306 (1953).
- [58] S. Chandrasekhar and D. D. Elbert, The instability of a layer of fluid heated below and subject to Coriolis forces. II, *Proc. R. Soc. London, Ser. A* **231**, 198 (1955).
- [59] G. Veronis, Cellular convection with finite amplitude in a rotating fluid, *J. Fluid Mech.* **5**, 401 (1959).
- [60] D. Fultz and Y. Nakagawa, Experiments on over-stable thermal convection in mercury, *Proc. R. Soc. London, Ser. A* **231**, 211 (1955).
- [61] Y. Nakagawa, Experimental observations of overstable cellular convection, *Proc. R. Soc. London, Ser. A* **253**, 212 (1959).
- [62] S. Chandrasekhar, The instability of a layer of fluid heated below and subject to the simultaneous action of a magnetic field and rotation, *Proc. R. Soc. London, Ser. A* **225**, 173 (1954).
- [63] S. Chandrasekhar, The instability of a layer of fluid heated below and subject to the simultaneous action of a magnetic field and rotation. II, *Proc. R. Soc. London, Ser. A* **237**, 476 (1956).
- [64] Y. Nakagawa, Experiments on the instability of a layer of mercury heated from below and subject to the simultaneous action of a magnetic field and rotation, *Proc. R. Soc. London, Ser. A* **242**, 81 (1957).
- [65] Y. Nakagawa, Experiments on the instability of a layer of mercury heated from below and subject to the simultaneous action of a magnetic field and rotation. II, *Proc. R. Soc. London, Ser. A* **249**, 138 (1959).
- [66] C. M. Vest and V. S. Arpaci, Overstability of a viscoelastic fluid layer heated from below, *J. Fluid Mech.* **36**, 613 (1969).
- [67] R. E. Khayat, Chaos and overstability in the thermal convection of viscoelastic fluids, *J. Non Newtonian Fluid Mech.* **53**, 227 (1994).
- [68] E. Guyon, P. Pieranski, and J. Salan, Overstability and inverted bifurcation in homeotropic nematics heated from below, *J. Fluid Mech.* **93**, 65 (1979).
- [69] J. R. Melcher and W. J. Schwarz Jr., Interfacial relaxation overstability in a tangential electric field, *Phys. Fluids* **11**, 2604 (1968).
- [70] J. Jukes, Gravitational resistive instabilities in plasma with finite Larmor radius, *Phys. Fluids* **7**, 52 (1964).
- [71] S. Moiseev and R. Sagdeev, Collisionless shock waves in a plasma in a weak magnetic field, *J. Nucl. Eng. Part C* **5**, 43 (1963).
- [72] F. F. Chen, "Universal" overstability of a resistive, inhomogeneous plasma, *Phys. Fluids* **8**, 1323 (1965).
- [73] G. Blumenthal, D. Lin, and L. Yang, On the overstability of axisymmetric oscillations in thin accretion disks, *Astrophys. J.* **287**, 774 (1984).
- [74] B. Roberts, Overstability and cooling in sunspots, *Astrophys. J.* **204**, 268 (1976).
- [75] E. Parker, Sunspots and the physics of magnetic flux tubes. IX-Umbral dots and longitudinal overstability, *Astrophys. J.* **234**, 333 (1979).
- [76] A. Castellanos, P. Atten, and M. Velarde, Oscillatory and steady convection in dielectric liquid layers subjected to unipolar injection and temperature gradient, *Phys. Fluids* **27**, 1607 (1984).
- [77] P. Martin and A. Richardson, Overstable electrothermal instabilities in a plane layer of dielectric liquid, *J. Electrostat.* **12**, 435 (1982).
- [78] E. N. Lorenz, Deterministic nonperiodic flow, *J. Atmos. Sci.* **20**, 130 (1963).
- [79] V. Il'in and B. Smorodin, Periodic and chaotic regimes of liquid dielectric convection in a horizontal capacitor, *Tech. Phys. Lett.* **31**, 432 (2005).
- [80] V. Il'in and B. Smorodin, Dynamics of electroconvective structures in a weakly conducting liquid, *J. Appl. Mech. Tech. Phys.* **49**, 362 (2008).
- [81] A. Taraut and B. Smorodin, Electroconvection in the presence of autonomous unipolar injection and residual conductivity, *J. Exp. Theor. Phys.* **115**, 361 (2012).
- [82] K. Luo, J. Wu, H.-L. Yi, and H.-P. Tan, Numerical investigation of heat transfer enhancement in electrothermo-convection in a square enclosure with an inner circular cylinder, *Int. J. Heat Mass Transfer* **113**, 1070 (2017).

- [83] K. Luo, T.-F. Li, J. Wu, H.-L. Yi, and H.-P. Tan, Mesoscopic simulation of electrohydrodynamic effects on laminar natural convection of a dielectric liquid in a cubic cavity, *Phys. Fluids* **30**, 103601 (2018).
- [84] I. Ginzburg, F. Verhaeghe, and D. d’Humières, Study of simple hydrodynamic solutions with the two-relaxation-times lattice Boltzmann scheme, *Commun. Comput. Phys.* **3**, 63 (2008).
- [85] D. d’Humières, Viscosity independent numerical errors for Lattice Boltzmann models: From recurrence equations to “magic” collision numbers, *Comput. Math. Appl.* **58**, 823 (2009).
- [86] I. Ginzburg, Truncation errors, exact and heuristic stability analysis of two-relaxation-times lattice Boltzmann schemes for anisotropic advection-diffusion equation, *Commun. Comput. Phys.* **11**, 1439 (2012).
- [87] K. Hayashi, R. Rojas, T. Seta, and A. Tomiyama, Immersed boundary-lattice Boltzmann method using two relaxation times, *J. Comput. Multiphase Flows* **4**, 193 (2012).
- [88] T. Seta, R. Rojas, K. Hayashi, and A. Tomiyama, Implicit-correction-based immersed boundary–lattice Boltzmann method with two relaxation times, *Phys. Rev. E* **89**, 023307 (2014).
- [89] H. Greenside and M. Cross, Stability analysis of two-dimensional models of three-dimensional convection, *Phys. Rev. A* **31**, 2492 (1985).
- [90] J. Boussinesq, *Théorie de l’écoulement tourbillonnant et tumultueux des liquides dans les lits rectilignes a grande section* (Gauthier-Villars, Paris, 1897), Vol. 1.
- [91] W. Worraker and A. Richardson, The effect of temperature-induced variations in charge carrier mobility on a stationary electrohydrodynamic instability, *J. Fluid Mech.* **93**, 29 (1979).
- [92] A. Castellanos, P. Atten, and M. Velarde, Electrothermal convection: Felici’s hydraulic model and the Landau picture of non-equilibrium phase transitions, *J. Non-Equilib. Thermodyn.* **9**, 10 (1984).
- [93] K. Luo, J. Wu, H.-L. Yi, and H.-P. Tan, Lattice Boltzmann modelling of electro-thermo-convection in a planar layer of dielectric liquid subjected to unipolar injection and thermal gradient, *Int. J. Heat Mass Transfer* **103**, 832 (2016).
- [94] R. Chicón, A. Castellanos, and E. Martin, Numerical modelling of Coulomb-driven convection in insulating liquids, *J. Fluid Mech.* **344**, 43 (1997).
- [95] Y. Guan, R. S. Vaddi, A. Aliseda, and I. Novosselov, Analytical model of electro-hydrodynamic flow in corona discharge, *Phys. Plasmas* **25**, 083507 (2018).
- [96] See Supplemental Material at <http://link.aps.org/supplemental/10.1103/PhysRevFluids.6.013702> for the details of the TRT LBM model, grid convergence analysis, error analysis, and the discussion of charge injection direction. Videos of Figs. 9 and 10 are also provided (2020).
- [97] A. Rodriguez-Luis, A. Castellanos, and A. Richardson, Stationary instabilities in a dielectric liquid layer subjected to an arbitrary unipolar injection and an adverse thermal gradient, *J. Phys. D: Appl. Phys.* **19**, 2115 (1986).
- [98] N. Goodnight, CUDA/OpenGL Fluid Simulation, NVIDIA Corporation (2007).
- [99] I. Ginzbourg and P. Adler, Boundary flow condition analysis for the three-dimensional lattice Boltzmann model, *J. Phys. II France* **4**, 191 (1994).
- [100] T. Krüger, H. Kusumaatmaja, A. Kuzmin, O. Shardt, G. Silva, and E. M. Viggen, *The Lattice Boltzmann Method* (Springer, Heidelberg, 2017).
- [101] I. Ginzburg, F. Verhaeghe, and D. d’Humières, Two-relaxation-time lattice Boltzmann scheme: About parametrization, velocity, pressure and mixed boundary conditions, *Commun. Comput. Phys.* **3**, 52 (2008).
- [102] S. Khirevich, I. Ginzburg, and U. Tallarek, Coarse-and fine-grid numerical behavior of MRT/TRT lattice-Boltzmann schemes in regular and random sphere packings, *J. Comput. Phys.* **281**, 708 (2015).
- [103] I. Ginzburg, L. Roux, and G. Silva, Local boundary reflections in lattice Boltzmann schemes: Spurious boundary layers and their impact on the velocity, diffusion and dispersion, *C. R. Mec.* **343**, 518 (2015).
- [104] I. Ginzburg, Prediction of the moments in advection-diffusion lattice Boltzmann method. II. Attenuation of the boundary layers via double- Δ bounce-back flux scheme, *Phys. Rev. E* **95**, 013305 (2017).